1 Oxygen Tracer Diffusion in Amorphous Hafnia Films for Resistive Memory

- 2 Dongjae Shin¹, Anton V. Ievlev², Karsten Beckmann^{3,4}, Jingxian Li¹, Pengyu Ren¹,
- 3 Nathaniel Cady³, Yiyang Li^{1#}
- 4 Materials Science and Engineering, University of Michigan, Ann Arbor, MI, USA
- ² Center for Nanophase Materials Science, Oak Ridge National Laboratory, Oak Ridge, TN, USA
- ⁶ College of Nanotechnology, Science and Engineering, University at Albany, Albany, NY, USA
- ⁴ NY CREATES, Albany, NY, USA
- 8 #Corresponding author: yiyangli@umich.edu

9 Abstract:

- 10 The oxygen diffusion rate in Hafnia (HfO₂)-based resistive memory plays a pivotal role in enabling
- 11 nonvolatile data retention. However, the information retention times obtained in HfO₂ resistive
- memory devices are orders of magnitude higher than the expected values obtained from oxygen
- diffusion measurements in HfO₂ materials. In this study, we resolve this discrepancy by conducting
- oxygen isotope tracer diffusion measurements in amorphous Hafnia (a-HfO₂) thin films. Our
- results show that the oxygen tracer diffusion in amorphous HfO₂ films is orders of magnitude lower
- than that of previous measurements on monoclinic hafnia (m-HfO₂) pellets. Moreover, oxygen
- tracer diffusion is much lower in denser a-HfO₂ films deposited by atomic layer deposition (ALD)
- than in less dense a-HfO₂ films deposited by sputtering. The ALD films yield similar oxygen
- diffusion times as experimentally measured device retention times, reconciling this discrepancy
- between oxygen diffusion and retention time measurements. More broadly, our work shows how
- 21 processing conditions can be used to control oxygen transport characteristics in amorphous
- 22 materials without long-range crystal order.

23 New Concept:

- 24 Amorphous hafnium oxide is one of the most important materials for microelectronics, with
- 25 applications in high-k gate dielectrics, resistive memory, and beyond. In this work, we
- 26 experimentally measured oxygen tracer diffusion on amorphous HfO₂ thin films for the first time
- 27 using isotope tracking. This differs from previous attempts to measure oxygen transport in
- amorphous HfO₂ that rely on computational simulations and indirect transient current analysis.
- Using this direct analysis, we show that the oxygen tracer diffusivity in amorphous HfO₂ shows a
- diffusion activation energy of \sim 1.5 eV, which is much higher than those previously measured. This
- 31 higher activation energy reconciles previous discrepancies in the predicted and experimentally
- 32 measured retention time of resistive memory devices. It furthermore shows that the oxygen
- diffusion in amorphous HfO₂ can be tuned using the processing conditions.

TOC Text:

34

- We quantified the oxygen tracer diffusion in amorphous hafnium oxide thin films. These tracer
- diffusion values are consistent with the experimentally measured retention times of hafnium
- 37 oxide resistive memory devices.

Introduction:

Resistive memories, or memristors, are electronic devices that switch their resistance states using applied currents and voltages. Such devices are highly promising for embedded memory, inmemory computing, and neuromorphic computing.^{1–4} Most resistive memories are composed of two-terminal structures with metal-insulator-metal structures.^{5,6} The insulators, often oxides, are critical in determining the properties of resistive memory devices.⁵

Valence-change memory using metal oxides like Ta₂O₅ or HfO₂ is the most promising type of resistive memory due to CMOS process compatibility, fast switching, and long retention, which exceeds 10 years at 85°C.^{5,6} Filament-based valence-change memory switches their resistance state through the electrochemical growth or dissolution of oxygen-deficient conducting filaments.⁷⁻¹² The information retention time depends on the stability of these oxygen-deficient filaments. Over time, the filaments dissolve due to the diffusion of oxygen ions into the conducting filaments, ultimately resulting in a loss of information, or retention failure.¹³⁻¹⁵ It is believed that the retention time is related to the characteristic oxygen diffusion time into the nanosized filament within the metal oxides.¹³⁻¹⁵ This is supported by large numbers of experimental measurements which show an Arrhenius dependence between the temperature and retention time.¹⁶⁻²²

Amorphous hafnia (a-HfO₂) is one of the most attractive candidates for resistive memory. Despite extensive research, there exists a vast discrepancy between the experimentally measured device retention time and the characteristic oxygen diffusion time inferred from materials characterization measurements. On the one hand, temperature-dependent device retention measurement suggests an oxygen activation energy between 1.2-1.6 eV.¹⁶⁻²¹ On the other hand, experimental measurements based on transient current analysis²³ and oxygen isotope tracer diffusion²⁴ suggest that the activation energy is only \sim 0.5 eV. This vast discrepancy in activation energy results in a greater than 8 order of magnitude difference between the predicted and experimentally realized retention time. For example, whereas experiments have shown >10 years of retention at 85°C¹⁶⁻²¹, the characteristic diffusion time based on previous oxygen diffusion measurements^{23,24} for a 10-nm filament is <10 seconds at the same temperature.

In this study, we reconcile this discrepancy by measuring the oxygen tracer diffusion of a-HfO₂ films, and compare them with the retention time of HfO₂ resistive memory devices fabricated using a 65-nm process on a 300-mm wafer. We reconcile the previous discrepancy by showing that

- the oxygen tracer diffusion of a-HfO₂ has a very similar Arrhenius activation energy (\sim 1.5 eV) as
- the device retention time (\sim 1.4 eV). We further show that atomic layer deposited (ALD) films have
- 3 about two orders of magnitude lower oxygen diffusivity than sputtered films, despite nominally
- 4 identical compositions and lack of long-range crystal order. We propose this difference to be a
- 5 result of the higher density of ALD films. These results provide precise information on the oxygen
- 6 diffusivities of a-HfO₂ thin films and reconciles previous discrepancies between device and
- 7 materials characterization results.

Results

Retention time for in-line HfO₂ resistive memory devices

Embedded HfO₂ resistive memory cells were fabricated on a 65-nm process on a 300 mm wafer at the Albany Nanotech Complex, Albany, NY (Fig. 1a,b). The resistive memory cells are built in the W-M1/Cu-M2 line and consists of a 30 nm TiN bottom electrode deposited by sputtering, a \sim 5.8 nm a-HfO₂ switching layer deposited by atomic layer deposition (ALD), and 6 nm Ti and 40 nm TiN top electrode deposited by sputtering. More details are given in the Experimental Methods. In addition, a 10 k Ω tungsten series resistor is patterned on the chip to limit the total current, thereby creating 1R1R structures (Fig. 1a).

Fig. 1c shows typical forming, SET, and RESET current-voltage profiles using direct current (DC) voltage sweeps with a 100 μ A current compliance (CC). The average HRS resistance is 351,000 Ω with a range of (98,000 \sim 1,200,000 Ω), and the average LRS resistance is 4,800 Ω with a range of (2,800 \sim 9,000 Ω). This resistance change is believed to result from the formation and dissolution of a conductive filament.

After switching, we measure the conductance after annealing a die with many devices at a given temperature. Supplementary Fig. S1 shows that the resistance increases over time, consistent with the dissolution of the conductive filament. Fig. 1d shows the retention time to failure of the low-resistance state at different temperatures; each temperature experiment contains six devices. Our results show that higher temperatures lead to a faster decrease in conductance, yielding retention failure.

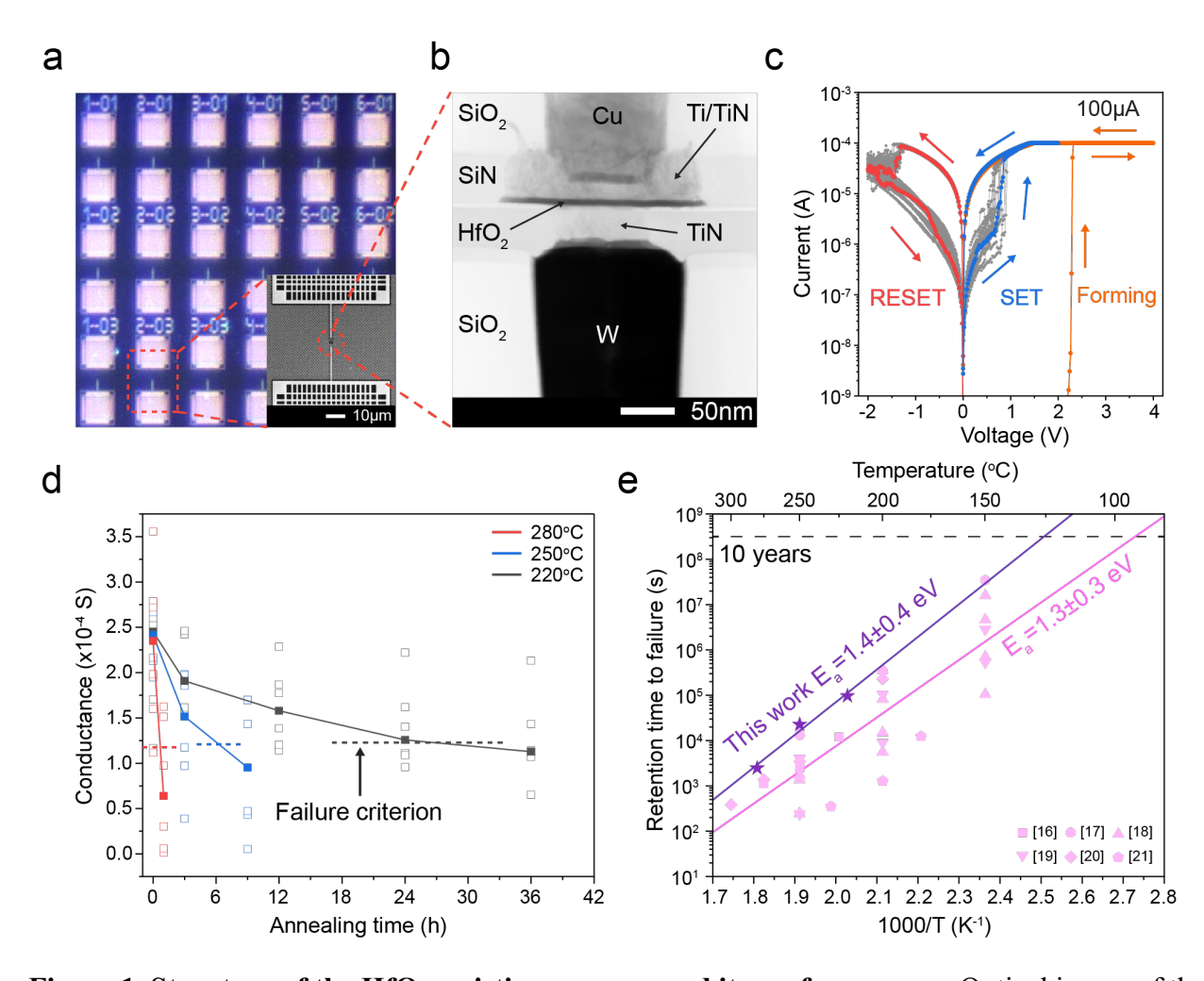


Figure 1. Structure of the HfO₂ resistive memory and its performance. a Optical image of the array of prepared HfO₂ resistive memories. The inset shows an SEM image of a HfO₂ resistive memory device. b Cross-section TEM image of a typical device c Typical current-voltage (I-V) curves of the HfO₂ resistive memory. d Evolution of the device conductance upon annealing at different temperatures. The empty squares are conductance values from the 6 devices at each annealing time and temperature (280°C red, 250°C blue, and 220°C black), while the solid squares represent medians calculated from the six conductance values at each annealing time and temperature. The dashed line indicates failure criteria defined as half the conductance value of the initial median. e Arrhenius plots of retention times to failure at different temperatures in this work (purple stars) and from previous research (pink symbols). The activation energy of the retention times in this work is 1.4 ± 0.4 eV, while that from the literature is 1.3 ± 0.3 eV. He errors indicate 2 standard errors in the Arrhenius equation fit.

In Fig. 1e, we plot the median retention time for our devices with purple stars. Our results suggest that the retention time t appear to follow the Arrhenius equation, $t = t_o exp\left(\frac{E_a}{kT}\right)$, where the activation energy E_a result from the migration enthalpy of oxygen (vacancy) defects. Based on our results, the activation energy equals 1.4 ± 0.4 eV (two standard errors).

We compare our results to that of previous work^{16–21} (Fig. 1e). There exists substantial variation in previous reports due to the use of different metallic electrodes, device geometries, and switching conditions (Supplementary Table S1-S2). By combining all previous data, we compute their activation energy to be 1.3 ± 0.3 eV, which is very similar to our 1.4 ± 0.4 eV. Consistent with previous reports, the extrapolated retention time exceeds 10 years at 85°C, satisfying the retention time requirement for nonvolatile memory applications.^{6,7}

We also conducted retention time measurements under different switching conditions. In Supplementary Fig. S2, we changed the current compliance to 50, 100, and 200 μ A. In Supplementary Fig. S3, we show the retention time after 1000 pulsed switching cycles. ²⁵ In Supplementary Fig. S4, we track the evolution of the HRS conductance. Finally, we conduct room temperature endurance in Supplementary Fig. S5. Except for the retention test at room temperature, all other devices showed LRS retention failure and produced slightly different activation energies between 1.2 and 1.5 eV, all within the uncertainty range. In Supplementary Fig. S6, we combined all retention times in our work and refitted them with the Arrhenius equation, resulting in the same value of activation energy, 1.4 ± 0.4 eV, as shown in Figure 1e.

Oxygen tracer diffusion in amorphous HfO₂

Next, we investigate oxygen tracer diffusion in amorphous HfO₂ thin films deposited by sputtering and by atomic layer deposition. To study oxygen tracer diffusion in sputtered HfO₂, we deposited tri-layer samples²⁶ comprised of an ¹⁸O-enriched HfO₂ layer sandwiched between natural-abundance oxygen HfO₂ oxide layers as shown in Fig. 2a; all three layers are nominally identical chemically (HfO₂). More details are given in Experimental Methods. Afterward, the trilayer samples are annealed at different temperatures and times to facilitate oxygen tracer diffusion Fig. 2a. Time of flight secondary ion mass spectrometry (ToF-SIMS) was used to depth-profile the oxygen isotope fraction for both unannealed "pristine" sample and annealed samples (Fig. 2b,c,d,e).²⁷ The annealed samples show broadened ¹⁸O profiles, signifying oxygen tracer diffusion. These diffusion profiles were fitted (blue line) to Crank's solution, which is an analytical solution to Fick's Laws of Diffusion.²⁸ Further details are described in Experimental Methods. X-ray diffraction (XRD) confirms that such samples are amorphous after these annealing conditions (Supplementary Fig. S7).

Fig. 2d shows the Arrhenius plots of oxygen tracer diffusion in sputtered HfO₂. The activation energy is 1.5 ± 0.1 eV (2 standard errors). This value is substantially higher than the previously reported activation energy of monoclinic HfO₂ (m-HfO₂, 0.5 ± 0.2 eV)²⁴, and nearly identical to the 1.4 ± 0.4 eV activation energy from the device retention measurements (Fig. 1e).

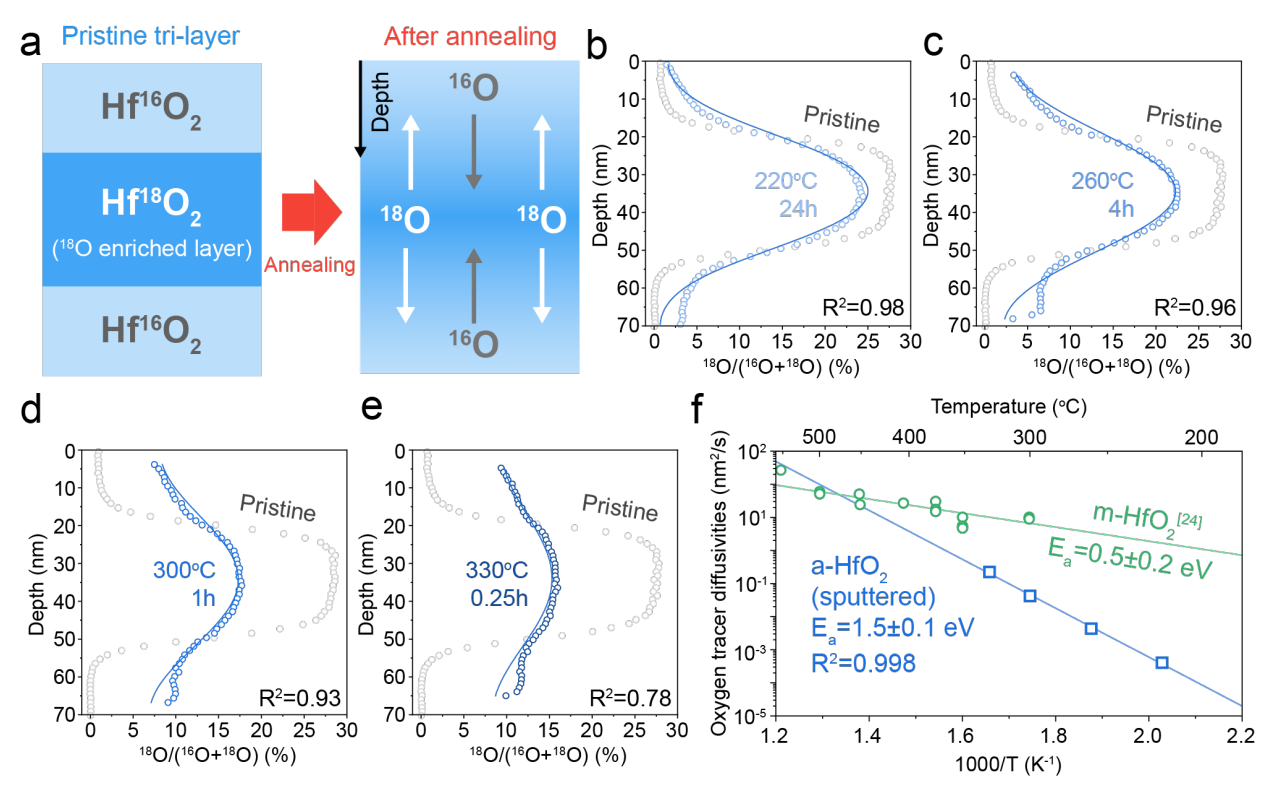


Figure 2. Oxygen tracer diffusivity measurement of sputtered HfO₂. a Schematic illustration of sample preparation for isotope tracer measurements. The middle layer was enriched with ~25% ¹⁸O (see Experimental Methods). **b,c,d,e** ¹⁸O isotope ratios against sample depth at different annealing temperatures and annealing times. (**b** 220°C 24h, **c** 260°C 4h, **d** 300°C 1h, and **e** 330°C 0.25h). Grey empty circles represent ¹⁸O fraction of samples before annealing (pristine tri-layer samples). The blue lines in each plot represent the fitting results. **f** Arrhenius plots of oxygen tracer diffusivities: sputtered amorphous HfO₂ (a-HfO₂, blue empty squares) and monoclinic HfO₂ (m-HfO₂, green empty circles) from ref. 24.

We next measure tracer diffusion in ALD-deposited HfO₂, which is widely used in resistive memory^{29,30} and as high-k dielectrics^{31,32}. Due to the challenges of introducing ¹⁸O oxygen into an ALD system, we instead sputter a 15-nm-thick ¹⁸O enriched HfO₂ above a 20-nm-thick ALD HfO₂ film (Fig. 3a). The ¹⁸O-enriched film was deposited using the same reactive DC sputtering as used in the sputtered films (Fig. 2a). XRD confirms that both layers are amorphous (Supplementary Fig. S8). XPS shows the two layers are chemically identical (Supplementary Fig. S9). Fig. 3b shows

cross-sectional scanning transmission electron microscopy (STEM) images of this sputtered/ALD bi-layer samples. Energy dispersive spectroscopy (EDS) shows that the Hf:O ratio of both films is about 1:2 (Supplementary Fig. S10), but the EDS maps show higher absolute intensity for both Hf and O in the ALD film (Fig. 3c). In Supplementary Fig. S11, X-ray reflectivity (XRR) analysis shows that ALD HfO₂ has a higher density (9.9 g cm⁻³) than sputtered HfO₂ (8.6 g cm⁻³), which is consistent with the higher Hf and O counts in the STEM-EDS maps (Fig. 3b). While both films are compositionally identical, the ALD films show higher density than the sputtered films.

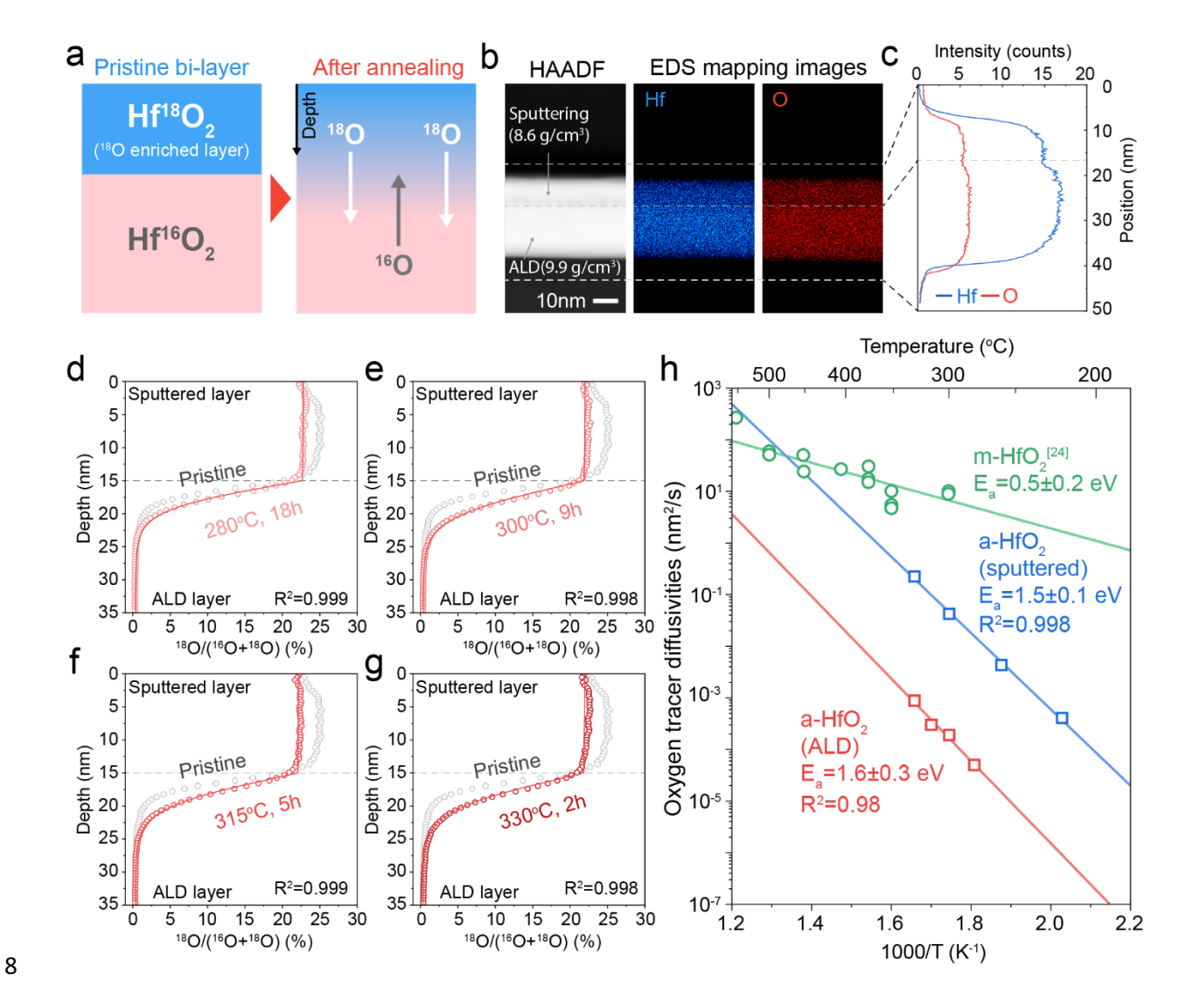


Figure 3. Oxygen tracer diffusion measurements for ALD HfO₂. a Schematic illustration of bilayer sample preparation for ToF-SIMS depth profiling. b STEM-HAADF image of cross sectional pristine bi-layer sample (left) and STEM-EDS mapping images of the bi-layer (mapping of Hf, middle, and O, right) c. STEM-EDS line scan results. Each curve indicates Hf (blue), and O (red) intensity along the depth of the sample. d,e,f,g ToF-SIMS depth profiling results of annealed

sample (red empty circles) and pristine sample (grey empty circles). Red lines show simulated depth. **h** The Arrhenius temperature plots of the measured oxygen diffusion in different types of HfO_2 . The activation energy of oxygen tracer diffusivities for ALD amorphous HfO_2 (a- HfO_2) is 1.6 ± 0.3 eV.

Next, we annealed these samples and depth-profiled the oxygen tracer concentrations using ToF-SIMS (Fig. 3d-g). These samples were annealed much longer than the sputtered ones in Fig. 2. While the oxygen tracer profile is relatively uniform in the top sputtered HfO₂, it undergoes a sharp gradient in the bottom ALD HfO₂. This result qualitatively suggests that the ALD film has much lower oxygen tracer diffusion than the sputtered film. To quantitatively solve for the oxygen diffusivity of the ALD, we use a finite-element simulation using Fick's Laws of Diffusion that uses the measured "pristine" experimental profile as the initial condition. We use this simulation to solve for the tracer diffusion coefficient that yields the best fit to experimental results (Fig. 3d-g). More details are given in the Experimental Methods and in Supplementary Fig. S12 and S13.

Fig. 3h plots the oxygen tracer diffusion of the ALD HfO₂ film alongside that of the sputtered amorphous HfO₂ (a-HfO₂) and the monoclinic HfO₂ (m-HfO₂) from ref. 24. The oxygen tracer diffusion activation energy of ALD a-HfO₂ was calculated to 1.6 ± 0.3 eV (2 standard errors), which is similar to the activation energy of the sputtered HfO₂. However, the absolute magnitude of tracer diffusion in the sputtered HfO₂ is about 300 times lower than that of the ALD films. We propose that this $300\times$ difference results from the much lower density of sputtered HfO₂ films compared to ALD ones (Fig. 3c, Supplementary Fig. S10& S11). This result is broadly in agreement with the "free volume" theory of diffusion in amorphous materials, whereby the ion diffusion pathway is enabled by the "free volume" that results from the non-close-packed structure of amorphous materials.³³ The difference in density between sputtered a-HfO₂ and ALD a-HfO₂ may have produced the slightly different activation energy (1.6 \pm 0.3 eV) compared to that of trilayer sample experiments (1.5 \pm 0.1 eV). However, given the margin of error, we are unable to conclude that these two activation energies are different from one another.

Comparison between Oxygen Tracer Diffusion and Device Retention Measurements

Our oxygen tracer diffusion measurements show that both ALD and sputtered HfO₂ have a very similar diffusion activation energy (\sim 1.5 eV), which is also very similar to the activation energies from the device retention measurements (\sim 1.4 eV). We next aim to correlate the absolute values between the characteristic diffusion time and the retention time. The characteristic diffusion

time τ is given by $\tau = \frac{L^2}{4D_0}$, where L is the characteristic diffusion length, and D_O is the oxygen diffusivity. Fig. 4a displays characteristic diffusion time as a function of the characteristic diffusion length based in ALD a-HfO₂ (red), sputtered a-HfO₂ (blue), and monoclinic HfO₂ (green) at 280°C.

We next analyze these characteristic diffusion time curves compared with the experimentally measured retention time at 280°C, designated by the dashed line. Our ALD films intersect at 0.7 nm; this value is very similar to experimentally measured filament diameters of below 5 nm in HfO_2^{34} resistive memories. In contrast, the oxygen tracer diffusion of the sputtered film does not intersect until 12 nm, while the value for monoclinic films does not intersect below 200 nm. Based on this result, we believe that the tracer diffusion values in ALD films best represent the oxygen diffusivity in HfO_2 resistive memory devices. However, the oxygen diffusivity in a filament may be different than that of a pristine film, which may explain the smaller estimated diffusion length (0.7 nm) compared to the expected filament radius of \sim 2 nm for this current compliance.³⁴

Finally, we compare the experimentally measured device retention time with the characteristic oxygen diffusion time obtained from different experimental measurements and computational simulations. Assuming a characteristic diffusion length of 0.7 nm, our results clearly show that the tracer diffusion coefficients obtained in our ALD films best match experimentally obtained retention times in resistive memory devices. Even if the true characteristic diffusion length is not 0.7 nm, our two tracer diffusion measurements are the only experimental results that match the activation energy slope of the resistive memory devices. The isotope tracer measurements are a more direct approach compared to transient current analysis for measuring oxygen diffusion. Additionally, our work quantified the tracer diffusion in amorphous rather than crystalline HfO₂ films, matching the amorphous films used in most HfO₂ resistive memory devices.

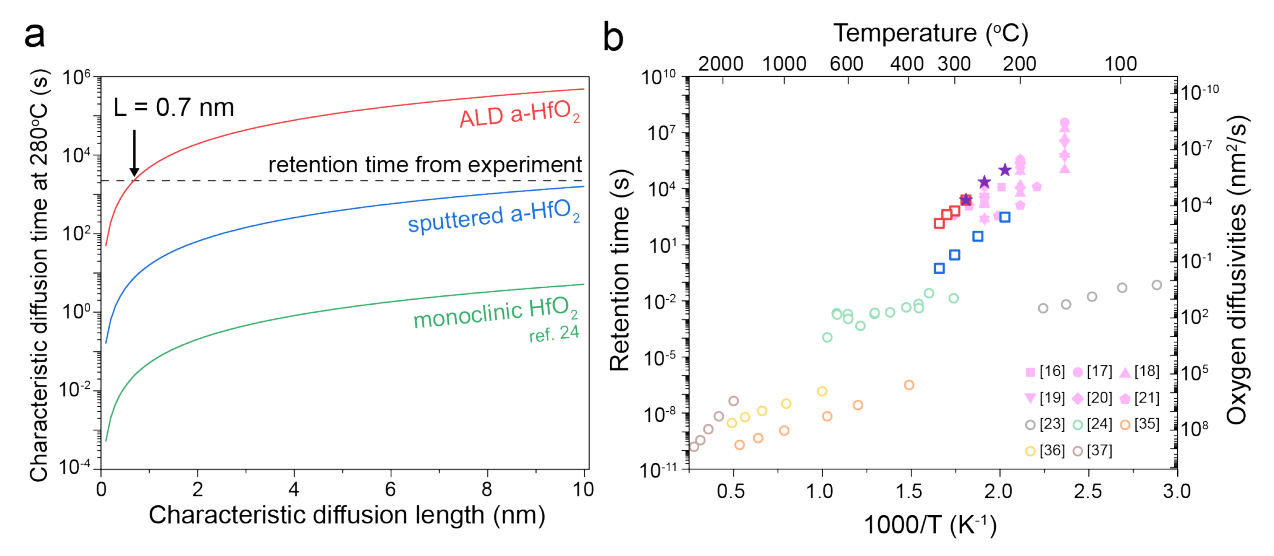


Fig 4. Comparison of retention and diffusion time. a The estimated diffusion length for the three types of HfO₂ tracer diffusion at 280°C. The dashed line indicates the experimentally obtained retention failure time. **b** The diffusion time estimates for L=0.7 nm based on different oxygen diffusion measurements (empty circles), including transient current analysis²³, isotope tracer diffusion²⁴, and molecular dynamic simulations^{35–37}. empty squares: sputtered a-HfO₂ (blue) and ALD a-HfO₂ (red). The experimentally obtained values for retention failure are given by purple stars (this work) and pink symbols (ref. 16-21).

Discussion

Our results show that the oxygen tracer diffusion of amorphous HfO_2 yields an activation energy of ~ 1.5 eV, which is qualitatively and quantitatively consistent with experimentally measured device retention times. In contrast, previous experiment work suggests that the activation energy is only ~ 0.5 eV²⁴, which yields many orders of magnitude differences in the predicted retention time. Our work unequivocally suggests that the oxygen diffusion activation energy in amorphous HfO_2 is in the ~ 1.5 eV range, enabling HfO_2 to be a resistive memory with long retention. This work also has important implications for amorphous- HfO_2 used in other devices, such as high-k gate dielectrics, or as electrolytes³⁸ or passivation layers³⁹ in electrochemical random-access memory.

An important consideration is the difference in the tracer diffusivity mechanisms of a crystalline and an amorphous material. In crystalline materials, the tracer diffusivity is given as the product of the defect (e.g., vacancy or interstitial) concentration and defect diffusivity.⁴⁰ As a result, the characteristic defect diffusion time is different from the characteristic tracer diffusion time. However, crystallographic point defects cannot be defined in amorphous materials.⁴¹ For this

reason, we propose that the characteristic oxygen tracer diffusion time is the correct metric for estimating the device retention time. As we show, the film density plays a large role in the oxygen tracer diffusivity.

It was recently shown that oxygen may undergo "uphill" diffusion against the concentration gradient because of spinodal decomposition.²⁶ However, these devices would fail from the highresistance to the low-resistance state. Our results show device failure from the low-resistance to the high-resistance state (Fig. 1) under our current compliance, which implies that the filaments dissolve over time. While our characteristic diffusion time model does not incorporate the thermodynamic factor, this thermodynamic factor is likely only a small correction to the diffusion time. Our work further assumes that oxygen diffusion in the suboxides that make up a filament is similar to oxygen diffusion in stoichiometric HfO₂ films. Preliminary investigation of oxygen diffusion in sputtered sub-stoichiometric HfO_{1.2} shows an activation energy ~1.2±0.4 eV, but an absolute magnitude similar to that of ALD films (Supplementary Fig. S9 & S14). The slight difference in the device retention activation energy and the tracer diffusion measurements may be because the devices contain a suboxide filament. The oxygen diffusivity of this suboxide, which may even be crystalline¹⁰, is likely different from that of an amorphous film deposited by sputtering or ALD. However, the overall range of the activation energies between our oxygen tracer diffusion (1.2-1.6 eV) and the device retention time (\sim 1.4 \pm 0.4 eV) shows that our results are much closer to the oxygen diffusion in Hafnia resistive memory devices, as opposed to previous measurements showing ~ 0.5 eV activation energy.

Conclusion

1

2

3

4

5

6

7

8

9

10

11

12

13

14

15

16

17

18

19

20

21

22

23

2425

26

27

28

29

30

In this work, we conducted the first oxygen tracer diffusion measurements in amorphous HfO₂, a technologically important material for resistive memory and high-k dielectrics. Our results show that the oxygen tracer diffusion is much lower than those measured using other methods, and qualitatively matches the retention times in HfO₂ resistive memory devices. Furthermore, our results show that the oxygen tracer diffusion in less-dense sputtered films is about 300 times higher than that of denser films deposited by atomic layer deposition, despite nominally identical chemical compositions. The oxygen tracer diffusion in atomic layer deposited films yield characteristic diffusion times that much more closely match the retention times in HfO₂ resistive memory devices.

Experimental Methods

HfO2 resistive memory fabrication

1

2

3

4

5

6

7

8

9

10

11

12

13

14 15

16

17

18

19

20

21

22

23

24

25

26

27

28

29

The characterized HfO₂ resistive memory was fabricated at the Albany NanoTech Complex by NY CREATES and the College of Nanotechnology, Science & Engineering (University at Albany). The devices are fabricated on a 300 mm wafer using a 65 nm back end of line (BEOL) process technology with custom modules embedding the resistive memory elements between tungsten and copper metallization 1 and 2, respectively (W-M1 and Cu-M2). The W-M1 interconnect is utilized to fabricate in-line resistors with $10 \text{ k}\Omega$ enabling on-chip current overshoot control during the resistive memory forming process. An inert TiN bottom electrode (BE) was structured above the W-M1 layer with a device diameter of 80 nm. The fabrication of the BE module was finished by a chemical mechanical polishing (CMP) process leaving an atomically flat contact for the deposition of the resistive memory stack. The 5.8 nm HfO₂ switching layer (SL) was deposited via atomic layer deposition (ALD) and followed by 6 and 40 nm of Ti and TiN via sputtering, which serves as the oxygen exchange layer (OEL) and top electrode (TE), respectively. The resistive memory stack was structured via a reactive ion etch (RIE) process to isolate the devices and an overlay of the SL, OEL, and TE above the BE of around 50 nm is maintained to avoid RIE edge effects during filament formation. The connection to the TE and W-M1 layer was accomplished using a via-first dual damascene process where the via etch and hard mask thickness are tuned to enable the bridging of the vertical height difference to connect the TiN top electrode and the W-M1 with a single patterning process. More details are given in our previous work. 42–47

Electrical measurements

The HfO₂ resistive memories were measured with Keithley 4200 semiconductor parameter analyzer. For DC switching measurements, the voltage bias was applied on the top electrode with the bottom electrode grounded. The current compliance was set at $100 \mu A$. For the forming step, a voltage sweep was conducted up to 4V, and, continuously, 20 cycles of RESET and SET cycles were applied with -2 V and 2V DC sweep, respectively. One representative switching behavior of HfO₂ resistive memory is displayed in Fig. 1c.

In Supplementary Fig. S3, we measured retention after 1000 cycles of pulse switching. Each cycle was composed of the following steps: RESET voltage was set to -3V, and SET voltage

was set to 2V. To read the resistance value of the device after RESET and SET operations, we included reading steps with a voltage of 0.15V. All pulse widths were fixed to $20\mu s$, and current compliance was set as $10\mu A$. Figure S3a displays a typical switching result of the pulsed switching.

After finishing switching cycles (DC or pulsed), the resistive switching devices were annealed under different temperatures (220°C, 250°C, and 280°C) for retention measurement. The annealing was conducted in a temperature and environmentally controlled probe station (Everbeing CG-196) under ~300 Torr of Ar. The conductance measurement was performed after cooling the memory devices at room temperature using voltage sweeps up to 0.1 V using the Keithley 4200.

Oxygen tracer diffusion measurement

Tri-layer (Hf¹⁶O₂/Hf¹⁸O₂/Hf¹⁶O₂) samples were deposited by using DC reactive sputtering using a 76-mm Hf metal target (AJA International Inc, 99.9% purity) via AJA Orion-8 Sputter System with three mass flow controllers. We used 100 W of sputter power while flowing 4 sccm of O₂ and 36 sccm of Ar under a totoal gas pressure of 5 mTorr. For the natural-abundance layer (Hf¹⁶O₂), we used a standard 99.999% purity O₂ cylinder with the natural O₂ abundance (~99.8 % ¹⁶O₂). For the 18O isotope enriched layer (Hf¹⁸O₂), the O₂ gas consisted of 1 sccm of 99%-enriched ¹⁸O₂ (Sigma-Aldrich, 99.9% purity) and 3 sccm of the natural abundance O₂ gas. Lastly, a 25 nm Pt layer was deposited on top of the tri-layer to prevent further oxidation under air. The prepared tri-layer samples were annealed under each condition under flowing inert Ar (~100 sccm) for 220°C 24 hours, 260°C 4 hours, 300°C 1 hour, and 330°C 0.25 hours using a Nextron CHH750 environmental probe station. The oxygen partial pressure of the chamber was measured to be around 3×10⁻⁶ bar using a Zirox ZR5 oxygen sensor.

Bi-layer (Hf¹⁸O₂/Hf¹⁶O₂) samples were prepared via atomic layer deposition (ALD) for the bottom layer (natural abundance) and reactive sputter deposition for the top layer (isotope-enriched). The bottom ALD layer was deposited with the Veeco Fiji ALD system in the Lurie Nanofabrication Facility (LNF) at the University of Michigan. Thermal ALD (200°C) was conducted for the bottom layer with precursor (Tetrakis(dimethylamino)hafnium, TDMAH). Subsequently, the ¹⁸O-enriched top layer was deposited with the same procedure as the enriched layer in the previous paragraph. The 60 nm protective Pt layer was sputtered to reduce oxidation under air. The prepared bi-layer samples were annealed with each condition (280°C 18 hours, 300°C)

9 hours, 315°C 5 hours, and 330°C 2 hours) under flowing Ar (~100 sccm) in the Nextron environmental probe station.

The time-of-flight secondary ion mass spectrometry (ToF-SIMS) analysis was performed using the ToF.SIMS.5-NSC instrument (ION.TOF GmbH) at the Center for Nanophase Materials Sciences at Oak Ridge National Laboratory. A Bi³⁺ liquid metal ion gun, operating at 30 keV energy, 0.5 nA current (DC mode), and with a spot size of approximately 120 nm, served as the primary source for chemical analysis. A Cs⁺ sputter ion gun was additionally used with operating at 1 keV energy and 70 nA current for depth profiling. The measurements were conducted in non-interlaced mode, with each analysis scan by Bi³⁺ ($100 \times 100 \, \mu m^2$) was succeeded by 2 seconds of sputtering with Cs⁺ ($300 \times 300 \, \mu m^2$). Low energy electron flood gun was used for charge compensation. Secondary ions were then analyzed using time-of-flight mass analyzers with a mass resolution of m/ $\Delta m = 100 \sim 300$ in the negative ion detection mode. Intensities of the peaks corresponding to $^{16}O^{-}$ and $^{18}O^{-}$ ions were further analyzed to calculate ^{18}O / (^{16}O + ^{18}O) ratio.

Materials characterization

Scanning transmission electron microscope (STEM) measurements were taken using a Thermo Fisher Talos F200X G2 at the University of Michigan. A 200 kV Field Emission Gun (FEG) scanning transmission electron microscope operated. The Velox software was used for STEM images and energy-dispersive X-ray spectroscopy (EDS) data acquisitions. The TEM specimen was prepared using a Thermo-Fisher Helios 650 Xe Plasma Focused Ion Beam (FIB). The final beam condition was set at 12 keV and 10 pA for the polishing of the specimen.

X-ray diffraction (XRD) and X-ray reflectivity (XRR) measurements were conducted using a Rigaku Smartlab X-ray diffractometer using a Cu K- α source. For XRD measurement, annealed bi-layer samples and annealed tri-layer samples were used. A 20nm layer of sputtered and ALD HfO₂ film were used for XRR density measurements.

X-ray photoelectron spectroscopy (XPS) was performed using Kratos Axis Ultra XPS system with a monochromatic Al source at room temperature.

Data Fitting

We used Crank's approach to solve for Fick's Law of Diffusion based on a separation of variables, with a zero-flux boundary condition:

$$\frac{\partial c}{\partial t} = D \frac{\partial c^2}{\partial x^2} \qquad (\text{Fick's 2}^{\text{nd law}})$$

Boundary condition:
$$\frac{\partial C}{\partial t}(0,t) = 0, \frac{\partial C}{\partial t}(L,t) = 0$$

x is depth of samples, and L represents tri-layer sample thickness (~70nm). We used the ToF-SIMS profile of the "pristine" sample as the initial condition; in this manner, we can account for the diffusion that occurs at room temperature between the sample fabrication and the ToF-SIMS measurements, around 10 days. Our solution is based on a Fourier Series decomposition of this "initial" condition, using the following analytical solutions:

$$C(x,t) = \sum_{n=0}^{\infty} A_n \cos\left(\frac{n\pi x}{L}\right) e^{-k\left(\frac{n\pi}{L}\right)^2 t}$$

11
$$A_n = \begin{cases} \frac{1}{L} \int_0^L C(x,0) \, dx &, n = 0 \\ \frac{2}{L} \int_0^L C(x,0) \cos\left(\frac{n\pi x}{L}\right) dx, n \neq 0 \end{cases}$$

where the "initial condition" C(x, 0) is the results of the experimentally-measured "pristine" film.

These analytical solutions provide good fits to the ToF-SIMS results of the sputtered samples (Fig. 2), where the oxygen diffusion *D* is nominally uniform across the sputtered tri-layer films, which are chemically identical. However, this solution would not be applicable for the bilayer films because the oxygen diffusion of the sputtered and ALD films is expected to differ.

To solve this problem, we used finite element methods with COMSOL Multiphysics 6.1, Transport of Dilute Species Module, to fit concentration profiles of bi-layer samples. This simulation contains two layers: the top sputtered layer uses the oxygen tracer diffusivities from the analytical solutions (Fig. 2), while the diffusivity of the ALD layer was fitted. We again use the measured concentration profiles of the "pristine" bi-layer samples as the initial condition.

Next, we simulated the concentration profile for each annealing condition and compared the simulated oxygen tracer profile with the experimental oxygen tracer profiles under the same

- annealing condition (Supplementary Fig. S12). We then computed the coefficient of determination
- 2 (R²) as a function of the fitted ALD diffusion values. The optimal oxygen tracer diffusivity is the
- 3 one with the highest R^2 (Supplementary Fig. S13).

Acknowledgements:

4

The work at the University of Michigan was supported by the National Science Foundation 5 6 under Grant no. ECCS-2106225 and startup funding from the University of Michigan College of Engineering. Y.L. acknowledges the support of an Intel Rising Star Gift. A.V.I. was partly 7 supported by the DOE Office of Science Research Program for Microelectronics Codesign 8 9 (sponsored by ASCR, BES, HEP, NP, and FES) through the Abisko Project, PM Robinson Pino (ASCR). The work at the State University of New York, Albany and NY CREATES was supported 10 by the Air Force Research Laboratory under agreement numbers FA8750-21-1-1018 and FA8750-11 21-1-1019. The U.S. Government may reproduce and distribute reprints for Governmental 12 purposes, despite any copyright notation. The views and conclusions expressed herein are solely 13 those of the authors and do not necessarily reflect the official policies or endorsements of the Air 14 Force Research Laboratory or the U.S. Government. The ToF-SIMS measurements were 15 conducted at the Center for Nanophase Materials Sciences, which is a DOE Office of Science User 16 17 Facility, and using instrumentation within ORNL's Materials Characterization Core provided by UT-Battelle, LLC under Contract No. DE-AC05-00OR22725 with the U.S. Department of Energy. 18 19 The authors acknowledge Wei D. Lu (University of Michigan), Yang Zhang (University 20 of Michigan), A. Alec Talin (Sandia National Laboratories), Jonathan Ihlefeld (University of 21 Virginia), Nicole Thomas (Intel), and Seung Hoon Sung (Intel) for helpful discussions on this research. The authors acknowledge the Michigan Center for Materials Characterization for use of 22 the instruments and staff assistance. Atomic laser deposition was conducted at the University of 23 24 Michigan, Lurie Nanofabrication Facility.

25 Conflict of Interest:

26 The authors declare no financial conflicts of interest.

27 Author Contributions

- D.S., J. L. and P. R. collected the memristor device data. J. L. conducted the TEM. D. S. and J. L.
- 29 conducted the thin film sample deposition. D.S. analyzed and fitted the data. A.V.I. conducted the
- 30 ToF-SIMS analysis. K.B. and N.C. developed and fabricated the memristor devices. Y. L.
- supervised the project. All authors contributed to writing, revising, and/or editing of the manuscript.

1 Data Availability

- 2 The data for the work can be accessed in the Materials Commons 2.0 Archive:
- 3 <u>https://doi.org/10.13011/m3-e9jr-6g69</u>. Any additional data (raw or processed) can be obtained
- 4 upon reasonable request to the corresponding author.

5 Reference

- 6 1 M. Lanza, A. Sebastian, W. D. Lu, M. Le Gallo, M.-F. Chang, D. Akinwande, F. M. Puglisi, H.
- N. Alshareef, M. Liu and J. B. Roldan, *Science*, 2022, **376**, eabj9979.
- 8 2J. J. Yang, D. B. Strukov and D. R. Stewart, *Nature Nanotech*, 2013, **8**, 13–24.
- 9 3D. Ielmini and H.-S. P. Wong, *Nat Electron*, 2018, 1, 333–343.
- 4Q. Xia and J. J. Yang, *Nat. Mater.*, 2019, **18**, 309–323.
- 5Z. Wang, H. Wu, G. W. Burr, C. S. Hwang, K. L. Wang, Q. Xia and J. J. Yang, Nat Rev Mater,
- 12 2020, **5**, 173–195.
- 6R. Dittmann, S. Menzel and R. Waser, *Advances in Physics*, 2021, **70**, 155–349.
- 7R. Waser, R. Dittmann, G. Staikov and K. Szot, Advanced Materials, 2009, 21, 2632–2663.
- 15 8D.-H. Kwon, K. M. Kim, J. H. Jang, J. M. Jeon, M. H. Lee, G. H. Kim, X.-S. Li, G.-S. Park, B.
- 16 Lee, S. Han, M. Kim and C. S. Hwang, *Nature Nanotech*, 2010, **5**, 148–153.
- 17 9 Y. Yang, X. Zhang, L. Qin, Q. Zeng, X. Qiu and R. Huang, *Nat Commun*, 2017, **8**, 15173.
- 18 10 Y. Zhang, G.-Q. Mao, X. Zhao, Y. Li, M. Zhang, Z. Wu, W. Wu, H. Sun, Y. Guo, L.
- 19 Wang, X. Zhang, Q. Liu, H. Lv, K.-H. Xue, G. Xu, X. Miao, S. Long and M. Liu, *Nat Commun*,
- 20 2021, **12**, 7232.
- 21 11 W. Banerjee, A. Kashir and S. Kamba, *Small*, 2022, **18**, 2107575.
- 22 12 M. Lanza, H. -S. P. Wong, E. Pop, D. Ielmini, D. Strukov, B. C. Regan, L. Larcher, M. A.
- Villena, J. J. Yang, L. Goux, A. Belmonte, Y. Yang, F. M. Puglisi, J. Kang, B. Magyari-Köpe, E.
- Yalon, A. Kenyon, M. Buckwell, A. Mehonic, A. Shluger, H. Li, T. Hou, B. Hudec, D.
- Akinwande, R. Ge, S. Ambrogio, J. B. Roldan, E. Miranda, J. Suñe, K. L. Pey, X. Wu, N.
- Raghavan, E. Wu, W. D. Lu, G. Navarro, W. Zhang, H. Wu, R. Li, A. Holleitner, U.
- Wurstbauer, M. C. Lemme, M. Liu, S. Long, Q. Liu, H. Lv, A. Padovani, P. Pavan, I. Valov, X.
- 28 Jing, T. Han, K. Zhu, S. Chen, F. Hui and Y. Shi, *Adv Elect Materials*, 2019, **5**, 1800143.
- 29 13 S. Larentis, C. Cagli, F. Nardi and D. Ielmini, *Microelectronic Engineering*, 2011, 88,
- 30 1119–1123.
- 31 14 S. Choi, J. Lee, S. Kim and W. D. Lu, *Appl. Phys. Lett.*, 2014, **105**, 113510.
- 32 D. Ielmini and R. Waser, Eds., Resistive switching: from fundamentals of nanoionic redox
- processes to memristive device applications, Wiley-VCH Verlag GmbH & Co. KGaA,
- 34 Weinheim, 2016.
- 35 16 M. Azzaz, E. Vianello, B. Sklenard, P. Blaise, A. Roule, C. Sabbione, S. Bernasconi, C.
- Charpin, C. Cagli, E. Jalaguier, S. Jeannot, S. Denorme, P. Candelier, M. Yu, L. Nistor, C.
- Fenouillet-Beranger and L. Perniola, in 2016 IEEE 8th International Memory Workshop (IMW),
- 38 IEEE, Paris, France, 2016, pp. 1–4.
- 39 Y. Y. Chen, M. Komura, R. Degraeve, B. Govoreanu, L. Goux, A. Fantini, N. Raghavan,
- S. Clima, L. Zhang, A. Belmonte, A. Redolfi, G. S. Kar, G. Groeseneken, D. J. Wouters and M.
- Jurczak, in 2013 IEEE International Electron Devices Meeting, IEEE, Washington, DC, USA,
- 42 2013, p. 10.1.1-10.1.4.

- 1 18 Y. Y. Chen, L. Goux, S. Clima, B. Govoreanu, R. Degraeve, G. S. Kar, A. Fantini, G.
- 2 Groeseneken, D. J. Wouters and M. Jurczak, *IEEE Trans. Electron Devices*, 2013, **60**, 1114–
- 3 1121.
- 4 19 Y. Y. Chen, R. Degraeve, S. Clima, B. Govoreanu, L. Goux, A. Fantini, G. S. Kar, G.
- 5 Pourtois, G. Groeseneken, D. J. Wouters and M. Jurczak, in 2012 International Electron
- 6 Devices Meeting, IEEE, San Francisco, CA, USA, 2012, p. 20.3.1-20.3.4.
- 7 20 B. Traore, P. Blaise, E. Vianello, H. Grampeix, S. Jeannot, L. Perniola, B. De Salvo and
- 8 Y. Nishi, *IEEE Trans. Electron Devices*, 2015, **62**, 4029–4036.
- 9 21 M. Zhao, H. Wu, B. Gao, Q. Zhang, W. Wu, S. Wang, Y. Xi, D. Wu, N. Deng, S. Yu, H.-
- 10 Y. Chen and H. Qian, in 2017 IEEE International Electron Devices Meeting (IEDM), IEEE,
- 11 San Francisco, CA, USA, 2017, p. 39.4.1-39.4.4.
- 12 Z. Wei, T. Takagi, Y. Kanzawa, Y. Katoh, T. Ninomiya, K. Kawai, S. Muraoka, S. Mitani,
- 13 K. Katayama, S. Fujii, R. Miyanaga, Y. Kawashima, T. Mikawa, K. Shimakawa and K. Aono,
- in *2011 International Electron Devices Meeting*, IEEE, Washington, DC, USA, 2011, p. 31.4.1-31.4.4.
- 16 23 S. Zafar, H. Jagannathan, L. F. Edge and D. Gupta, *Appl. Phys. Lett.*, 2011, **98**, 152903.
- 17 24 M. P. Mueller and R. A. De Souza, *Appl. Phys. Lett.*, 2018, **112**, 051908.
- 18 25 Y.-F. Chang, J. A. O'Donnell, T. Acosta, R. Kotlyar, A. Chen, P. A. Quintero, N. Strutt, O.
- Golonzka, C. Connor and J. Hicks, in *2020 IEEE International Reliability Physics Symposium* (IRPS), IEEE, Dallas, TX, USA, 2020, pp. 1–4.
- 21 26 J. Li, A. Appachar, S. Peczonczyk, E. Harrison, B. Roest, A. Ievlev, R. Hood, S. Yoo, K.
- Sun, A. Talin, W. Lu, S. Kumar, W. Sun, and Y. Li Thermodynamic origin of nonvolatility in
- resistive switching, 2022. Preprint (In Review): https://doi.org/10.21203/rs.3.rs-2365752/v1
- 24 27 R. A. De Souza and M. Martin, *Phys. Status Solidi* (c), 2007, **4**, 1785–1801.
- 25 28 J. Crank, *The mathematics of diffusion*, Univ. Pr, Oxford, 2. ed., repr., 2011.
- 26 29 H. Kim, H.-B.-R. Lee and W.-J. Maeng, *Thin Solid Films*, 2009, **517**, 2563–2580.
- 27 30 A. S. Sokolov, Y.-R. Jeon, S. Kim, B. Ku, D. Lim, H. Han, M. G. Chae, J. Lee, B. G. Ha and C. Choi, *Applied Surface Science*, 2018, **434**, 822–830.
- 29 31 K. Mistry, R. Chau, C.-H. Choi, G. Ding, K. Fischer, T. Ghani, R. Grover, W. Han, D.
- Hanken, M. Hattendorf, J. He, C. Allen, J. Hicks, R. Huessner, D. Ingerly, P. Jain, R. James, L.
- Jong, S. Joshi, C. Kenyon, K. Kuhn, K. Lee, C. Auth, H. Liu, J. Maiz, B. McIntyre, P. Moon, J.
- Neirynck, S. Pae, C. Parker, D. Parsons, C. Prasad, L. Pipes, B. Beattie, M. Prince, P. Ranade,
- T. Reynolds, J. Sandford, L. Shifren, J. Sebastian, J. Seiple, D. Simon, S. Sivakumar, P. Smith,
- D. Bergstrom, C. Thomas, T. Troeger, P. Vandervoorn, S. Williams, K. Zawadzki, M. Bost, M.
- Brazier, M. Buehler and A. Cappellani, in 2007 IEEE International Electron Devices Meeting,
- 36 IEEE, Washington, DC, 2007, pp. 247–250.
- 37 32 J. H. Choi, Y. Mao and J. P. Chang, Materials Science and Engineering: R: Reports,
- 38 2011, **72**, 97–136.
- 39 33 F. Faupel, W. Frank, M.-P. Macht, H. Mehrer, V. Naundorf, K. Rätzke, H. R. Schober, S.
- 40 K. Sharma and H. Teichler, *Rev. Mod. Phys.*, 2003, **75**, 237–280.
- 41 34 U. Celano, L. Goux, R. Degraeve, A. Fantini, O. Richard, H. Bender, M. Jurczak and W.
- 42 Vandervorst, *Nano Lett.*, 2015, **15**, 7970–7975.
- 43 35 S. Clima, Y. Y. Chen, R. Degraeve, M. Mees, K. Sankaran, B. Govoreanu, M. Jurczak, S.
- De Gendt and G. Pourtois, *Applied Physics Letters*, 2012, **100**, 133102.
- 45 36 M. Schie, M. P. Müller, M. Salinga, R. Waser and R. A. De Souza, *The Journal of*
- 46 *Chemical Physics*, 2017, **146**, 094508.

- 1 37 G. Broglia, G. Ori, L. Larcher and M. Montorsi, *Modelling Simul. Mater. Sci. Eng.*, 2014,
- **2 22**, 065006.
- 3 38 S. Kim, T. Todorov, M. Onen, T. Gokmen, D. Bishop, P. Solomon, K.-T. Lee, M. Copel,
- D. B. Farmer, J. A. Ott, T. Ando, H. Miyazoe, V. Narayanan and J. Rozen, in 2019 IEEE
- 5 International Electron Devices Meeting (IEDM), IEEE, San Francisco, CA, USA, 2019, p.
- 6 35.7.1-35.7.4.
- 7 39 D. S. Kim, V. J. Watkins, L. A. Cline, J. Li, K. Sun, J. D. Sugar, E. J. Fuller, A. A. Talin
- 8 and Y. Li, *Adv Elect Materials*, 2022, 2200958.
- 9 40 R. A. De Souza, *Adv. Funct. Mater.*, 2015, **25**, 6326–6342.
- 10 41 R. De Souza and G. Harrington, *Nat. Mater.*, 2023, **22**, 794–797.
- 42 M. Liehr, K. Beckmann and N. Cady, in 2022 IEEE 31st Microelectronics Design & Test
 Symposium (MDTS), IEEE, Albany, NY, USA, 2022, pp. 1–6.
- 43 M. Abedin, N. Gong, K. Beckmann, M. Liehr, I. Saraf, O. Van Der Straten, T. Ando and
 N. Cady, *Sci Rep*, 2023, 13, 14963.
- 15 44 J. Hazra, M. Liehr, K. Beckmann, M. Abedin, S. Rafq and N. Cady, in 2021 IEEE
- 16 International Memory Workshop (IMW), IEEE, Dresden, Germany, 2021, pp. 1–4.
- 17 45 K. Beckmann, W. Olin-Ammentorp, G. Chakma, S. Amer, G. S. Rose, C. Hobbs, J. V.
- Nostrand, M. Rodgers and N. C. Cady, J. Emerg. Technol. Comput. Syst., 2020, 16, 1–18.
- 19 46 K. Beckmann, N. Suguitan, J. Van Nostrand and N. C. Cady, Semicond. Sci. Technol.,
- 20 2019, **34**, 105021.

23

- 21 47 K. Beckmann, J. Holt, W. Olin-Ammentorp, Z. Alamgir, J. Van Nostrand and N. C. Cady,
- 22 Semicond. Sci. Technol., 2017, **32**, 095013.